EUROFUSION WPS1-PR(16) 16687

J. M. Garcia-Regana et al.

Electrostatic potential variation on the flux surface and its impact on impurity transport

Preprint of Paper to be submitted for publication in
Nuclear Fusion

This work has been carried out within the framework of the EUROfusion Consortium and has received funding from the Euratom research and training programme 2014-2018 under grant agreement No 633053. The views and opinions expressed herein do not necessarily reflect those of the European Commission.

Electrostatic potential variation on the flux surface and its impact on impurity transport

J. M. García-Regaña[1,2], C. D. Beidler[2], R. Kleiber[2], P. Helander[2], A. Mollén[2], J. A. Alonso[1], M. Landreman[3], H. Maaßberg[2], H. M. Smith[2], Y. Turkin[2] and J. L. Velasco[1]

[1] Laboratorio Nacional de Fusión Ciemat, Av. Complutense 40, 28040 Madrid, Spain
[2] Max-Planck-Institut für Plasmaphysik, Wendelsteinstr. 1, 17491 Greifswald, Germany
[3] Institute for Research in Electronics and Applied Physics, University of Maryland, College Park, Maryland 20742, USA

E-mail: jose.regana@ciemat.es

Abstract. The particle transport of impurities in magnetically confined plasmas under some conditions finds neither quantitatively nor qualitatively a satisfactory theory-based explanation. This compromises the successful realization of thermonuclear fusion for energy production since its accumulation is known to be one of the causes that leads to the plasma radiative collapse.
In standard reactor-relevant conditions this accumulation is in stellarators intrinsic to the lack of toroidal symmetry, and results from the radially inwards neoclassical electric field predicted by the theory. The high charge state of the impurities particularly makes its transport more sensitive to the electric fields. Consequently the short length scale turbulent electrostatic potential or its long wave-length variation on the flux surface Φ_1, that the standard neoclassical approach usually neglects, can possibly shed some light on the experiments where a satisfactory explanation has not yet been found, e.g. [1, 2],
In the present work we have considered different stellarator configurations and assessed the impact that Φ_1 has on the radial particle transport of selected impurities. The results for LHD show that Φ_1 can strongly modify it, resulting in large deviations of the level of inward impurity flux predicted by the standard neoclassical theory in most cases. In Wendelstein 7-X, on the contrary, Φ_1 is significantly smaller and, for the parameters considered, its effect only appreciable for high charged impurities. Finally, in TJ-II the potential variation leads to appreciable changes on the impurity radial flux although not to the extent its large amplitude might lead one to think. The dependence on the chosen parameters and open questions for future developments are discussed.

1. Introduction

When a plasma is confined by means of a magnetic field, $\mathbf{B}$, an electric field, $\mathbf{E} = -\nabla\Phi$, invariably also arises. Because of the high conductivity of the plasma along the magnetic field, the electric field is mostly perpendicular to $\mathbf{B}$, but also has a small component

within the flux surface. In other words, the electrostatic potential can be written as $\Phi = \Phi_0(r) + \Phi_1$, where $\Phi_0(r)$ is constant on magnetic surfaces (labelled by the coordinate r) and Φ_1 varies over such surfaces. This is true both in axisymmetric and non-axisymmetric magnetic fields, but the mechanisms creating the electric field are very different.

1.1. Radial electric field

We shall refer to the electric field perpendicular to the flux surface as *radial*, $\mathbf{E}_0 = -\nabla\Phi_0 = E_r\nabla r$, and first note that, in an axisymmetric magnetic field such as that of a tokamak, plasma transport is independent of E_r to a good approximation. Both the collisional transport and that arising from gyrokinetic turbulence are independent of the radial electric field to lowest order in the normalised gyroradius, $\rho_* = \rho_i/L$, and the Mach number $M = V/v_{Ti}$, which we take to be much smaller than unity [3, 4]. Here, $\rho_i = v_{Ti}/\Omega_i$ denotes the ion gyroradius, v_{Ti} the ion thermal velocity, Ω_i the gyrofrequency, L the macroscopic length scale (such as the major radius) and V the plasma flow velocity, the perpendicular component of which for the bulk ions with mass m_i, density n_i and pressure p_i is equal to

$$\mathbf{V}_\perp = \frac{(\mathbf{E} - \nabla p_i/n_i e) \times \mathbf{B}}{B^2}$$

and is thus controlled by the radial electric field if this is large enough. If $\mathbf{B}$ is axisymmetric, then the effect of E_r on the transport is small in the parameters ρ_* and M. This property is usually referred to as intrinsic (or automatic) ambipolarity. There is a simple reason for it: in a coordinate system rotating toroidally with a velocity $\mathbf{U}$, the electric field is equal to $\mathbf{E} + \mathbf{U} \times \mathbf{B}$ (where $\mathbf{E}$ denotes the field in the laboratory frame) and its radial component can be made to vanish by choosing $\mathbf{U}$ appropriately. In such a frame, the physics is the same as in the laboratory frame, except that there is a centrifugal force and a Coriolis force. The former is quadratic in the Mach number and therefore does not matter to first order in M, and the Coriolis force on a mass m moving with velocity $\mathbf{v}$ is equal to

$$\mathbf{F}_c = 2m\mathbf{v} \times \boldsymbol{\omega},$$

where $\boldsymbol{\omega}$ is the angular rotation frequency corresponding to the velocity $\mathbf{U}$. Because it has the same form as the Lorentz force on a charge q, it can be accounted for in the kinetic equation by adjusting the magnetic field according to

$$\mathbf{B} \to \mathbf{B} + \frac{2m}{q}\boldsymbol{\omega},$$

which is a very small change, $m\omega/qB \sim \rho_* M$. The effects of both the centrifugal and Coriolis forces are thus quadratic in the small parameters ρ_* and M. The kinetic equation for the plasma in the rotating frame is thus locally identical to that in the laboratory frame to first order in these parameters, and we conclude that the radial

electric field cannot affect the behaviour of the plasma in this order, at least not locally. (A sheared electric field can however have an effect on turbulence, and even an unsheared field can affect turbulence through non-local effects.)

In a non-axisymmetric magnetic field, the neoclassical transport is not ambipolar unless the field is quasi-symmetric, and the radial electric field is set by the requirement that the ion and electron particle fluxes across magnetic surfaces should be equal. However, the turbulent transport remains ambipolar even in non-axisymmetric fields if the turbulent fluctuations satisfy the gyrokinetic equations [4, 5]. The radial electric field is determined by neoclassical transport processes alone in non-axisymmetric and non-quasisymmetric magnetic fields [6] (an exception occurs on small radial scales comparable to the ion gyroradius, on which zonal flows may arise). This is in stark contrast to tokamaks, where the radial electric field is controlled by the transport of angular momentum, which is a higher-order process in ρ_* and therefore difficult to calculate, both in neoclassical and in gyrokinetic theory [7, 8].

In a stellarator, the radial electric field affects the neoclassical particle flux of each species a, which is governed by a transport law of the form

$$\langle \mathbf{\Gamma}_a \cdot \nabla r \rangle = -n_a \sum_b \left[D_1^{ab} \left(\frac{\mathrm{d} \ln n_b}{\mathrm{d}r} - \frac{q_b E_r}{T_b} \right) + D_2^{ab} \frac{\mathrm{d} \ln T_b}{\mathrm{d}r} \right], \tag{1}$$

where n_a denotes the density, T_a the temperature, $q_a = Z_a e$ the charge, and the sum is taken over all the species b present in the plasma. The terms with $b \neq a$ are due to the friction along $\mathbf{B}$ between the different species and are in stellarators usually negligible in comparison with the $b = a$ term at low collisionality. The terms with $b \neq a$ are therefore usually neglected in numerical codes [9]. The term proportional to the radial electric field is absent in axisymmetric systems but tends to cause relatively strong inward transport of highly charged impurities in stellarators, since E_r is usually negative.

1.2. Electric field within flux surfaces

The electric field within the magnetic surface, $\mathbf{E}_1 = -\nabla \Phi_1$, has received less attention in the literature. It is usually relatively small, but can have a substantial effect on highly charged impurities with charge numbers $Z \gg 1$. There are a few different mechanisms that can cause such a field to appear.

First, axisymmetric plasmas can rotate rapidly in the toroidal direction. In tokamaks with strong neutral-beam injection, the Mach number can become order unity, so that the centrifugal force becomes comparable to the pressure gradient. The bulk ions are then driven to the outboard side of each flux surface, and a poloidal electric field (directed toward the inboard side) arises to maintain quasineutrality [10, 11]. For heavy impurities, the force from this electric field is smaller than the centrifugal force, so the impurities are pushed to the outboard side of the flux surface.

Second, fast ions from neutral-beam injection or ion-cyclotron-resonance-heating

(ICRH) usually have anisotropic pressure and are therefore not evenly distributed over flux surfaces. For instance, ICRH-heated minority ions reside mostly on the outboard side, and a poloidal electric field directed to the inboard side is again required to make the plasma quasineutral. Impurity ions therefore accumulate on the inboard side [12].
Third, even without fast rotation or fast ions, the plasma has a *natural* tendency to produce a poloidal electric field. In a tokamak, this electric field is relatively small, as can be seen from the ρ_*-expansion of the drift kinetic equation, which we write as

$$\dot{\mathbf{R}} \cdot \nabla f_a + \dot{v}_\parallel \frac{\partial f_a}{\partial v_\parallel} = C_a(f_a),$$

where the derivatives are taken at constant magnetic moment, $\mu = m_a v^2/2B$, and $\mathbf{R}$ denotes the guiding centre position. To zeroth order in ρ_*, there is no magnetic drift and the $\mathbf{E} \times \mathbf{B}$ drift can be transformed away as described above, so that

$$\dot{\mathbf{R}} = v_\parallel \mathbf{b},$$

$$\dot{v}_\parallel = -\mu \mathbf{b} \cdot \nabla B - \frac{Z_a e}{m_a} \mathbf{b} \cdot \nabla \Phi,$$

where $\mathbf{b} = \mathbf{B}/B$, m_a denotes the mass. The electrostatic potential is determined by the quasineutrality condition

$$\sum_a Z_a e \int f_{0a} d^3 v = 0,$$

and one finds that Φ_1 vanishes in this order [3], implying that $e\Phi_1/T \sim \rho_*$, where T is the temperature. From the first-order kinetic equation, one finds that the electrostatic potential is small in the collisionality, too, so that $e\Phi_1/T \sim \rho_* \nu_*$, where $\nu_* = \nu L/v_T$ denotes the collisionality and v_T the thermal speed [13].
In a stellarator, the situation is more complicated, and the poloidally (and toroidally) varying part of the electrostatic potential can be significantly larger. This has to do with the mechanism through which the radial electric field causes the cross-field transport to be ambipolar. The diffusion coefficients in equation 1 tend to be larger for the ions than for the electrons, so an inward-pointing radial electric field arises to reduce the flux of the ions and enhance that of the electrons to ensure ambipolarity. It is clear from equation 1 that the required electrostatic potential must be of order

$$\frac{e\Phi_0}{T} \sim 1.$$

On the level of particle trajectories, the reduction of the ion transport occurs because $\mathbf{E}_0 \times \mathbf{B}$ drift convects locally trapped ions poloidally around the torus, and thereby limits the radial step size in their collisional random walk. However, as explained in Refs. [14, 15], the radial width of the resulting trajectories is such that the density develops an in-out asymmetry on each flux surface, and to keep the plasma quasineutral, a poloidal electric field is established. In these references, the electric field was calculated

in the case of circular flux surfaces and was found not to scale with ρ_*, but roughly as

$$\frac{e\Phi_1}{T} \sim \frac{f_T \Delta B}{B}, \tag{2}$$

where ΔB is the variation of the magnetic field strength over the flux surface and f_T the fraction of trapped particles. This ratio is usually smaller than unity by some considerable (but not very large) margin, so that the variation of the electrostatic potential over flux surfaces is modest. This variation causes an additional $\mathbf{E}_1 \times \mathbf{B}$ drift across the flux surfaces which adds to the radial neoclassical transport, but the effect is not very large for the bulk ions and electrons [15]. For moderate to highly charged impurity ions, the effect can however be substantial.

1.3. Effect on impurity ions

The neoclassical transport of impurity ions has long been an issue of concern. Since the total transport must be ambipolar, the outward flux of bulk ions must necessarily either be accompanied by a similar electron flux or be balanced by an inward impurity flux. In tokamaks, the neoclassical electron transport practically vanishes, and in stellarators, the inward electric field makes the second term in equation 1 for impurities a factor Z_a larger than the other terms, so in both cases impurity accumulation tends to arise.
However, standard neoclassical theory assumes that all densities are constant over flux surfaces. Since the density tends to follow a Boltzmann distribution function within such surfaces,

$$n_a \propto \exp\left(-\frac{Z_a e\Phi_1}{T_a}\right),$$

in particular impurities with $Z_a \gg 1$ will tend to develop in-surface density variations in response to Φ_1. Highly charged impurities also experience a relatively large parallel friction force from the bulk ions, which also leads to a density variation. Furthermore, the collisionless orbits also tend to get modified by Φ_1, because the electric force along the field $Z_a e\mathbf{b}\cdot\mathbf{E}_1$ can compete with the mirror force ,

$$\frac{Ze\nabla_\parallel \Phi_1}{\mu \nabla_\parallel B} \sim \frac{Ze\Phi_1}{T}, \tag{3}$$

if $Zf_T\Delta B/B$ is of order unity. Electrostatic trapping is then as important as magnetic trapping. For these reasons, the neoclassical transport of heavy impurity ions can be affected significantly, both in tokamaks [16, 17, 18] and in stellarators [19, 20]. In tokamaks, the most noticable effects arise because of the potential variation caused by anisotropic fast ions, which can dramatically affect both the size and the magnitude of the transport [21].

2. Mathematical and numerical treatment

It is not entirely straightforward to construct an ordering of the various terms in the drift kinetic equation that is both rigorous and adequately describes the effect

of the electric field whilst still retaining the radially local character of conventional neoclassical transport theory. Different alternatives were recently discussed and compared numerically by Landreman *et al* [22], who however neglected Φ_1 in their treatment. We shall adopt their most complete model (called *full trajectories* in their paper), and extend it to include Φ_1. The full equations of guiding center motion are

$$\dot{\mathbf{R}} = v_\parallel \mathbf{b} + \frac{\mathbf{b} \times \nabla \Phi}{B} + \mathbf{v}_d \tag{4}$$

$$\dot{v}_\parallel = -\frac{1}{m_a v_\parallel} \dot{\mathbf{R}} \cdot (\mu \nabla B + Z_a e \nabla \Phi), \tag{5}$$

$$\dot{\mu} = 0. \tag{6}$$

and the simplified local ones are

$$\dot{\mathbf{R}} = v_\parallel \mathbf{b} + \frac{\mathbf{b} \times \nabla \Phi_0}{B}, \tag{7}$$

$$\dot{v}_\parallel = -\frac{\mu}{m_a} \mathbf{b} \cdot \nabla B - \frac{v_\parallel}{B^2} (\mathbf{b} \times \nabla B) \cdot \nabla \Phi_0 - \frac{Z_a e}{m_a} \mathbf{b} \cdot \nabla \Phi_1, \tag{8}$$

$$\dot{\mu} = 0. \tag{9}$$

2.1. The code EUTERPE and solution of the drift kinetic equation

For the integration of the equations of motion and calculation of the radial impurity fluxes and electrostatic potential variation Φ_1, the Monte Carlo δf Particle-in-Cell (PIC) code EUTERPE [24] has been employed. The details of the numerical method can be found in Ref. [25], but succinctly it can be summarised as follows.

The method considers a splitting of the distribution function f for any kinetic species present in the problem as $f = f_0 + \delta f$, prescribing an analytically known part f_0 and a departure from this δf, which is represented by a set of Monte-Carlo markers. The equation to solve for the δf part can be expressed in all generality as

$$\frac{\mathrm{d}\delta f}{\mathrm{d}t} = -\frac{\mathrm{d}f_0}{\mathrm{d}t} + C(f), \tag{10}$$

with $C(f)$ the collision operator.

The code is multi-species, the gyro-kinetic version is electro-magnetic and considers the full flux surface and radial domain. The neoclassical version applied to the present problem is local instead, as no drift across the flux surface remains in equation 7, and binds the radial position of each marker to its value at the initialization. To solve equation 10 a standard two weight scheme [26, 27] is applied, with δf and f_0 represented by

$$\delta f = \sum_p w_{1p} \delta \left(\mathbf{z} - \mathbf{z}_p \right) \mathcal{J}^{-1} \left(\mathbf{z} \right), \tag{11}$$

$$f_0 = \sum_p w_{2p} \delta \left(\mathbf{z} - \mathbf{z}_p \right) \mathcal{J}^{-1} \left(\mathbf{z} \right), \tag{12}$$

with $\mathbf{z} = \{\mathbf{R}, v_\parallel, \mu\}$ the phase space coordinates, δ the Dirac delta function, w_1 and w_2 the marker weights, p the marker index, $\mathcal{J}$ the phase space Jacobian. Denoting the full guiding centre equations 4 to 6 by $\dot{\mathbf{z}}$ and the reduced local ones 7-9 by $\dot{\mathbf{z}}_0$, the following expressions for the evolution of the marker weights can be derived,

$$\dot{w}_{1p} = -\frac{w_{2p}}{f_0} \left(\dot{z}^i \frac{\partial f_0}{\partial z^i} \right), \tag{13}$$

$$\dot{w}_{2p} = \frac{w_{2p}}{f_0} \left(z_0^i \frac{\partial f_0}{\partial z^i} \right), \tag{14}$$

where the summation over repeated indices is assumed. In eqs. 13 and 14 the collision operator is assumed to consist only of the test particle term $C(\delta f, f_0)$ describing the collisions of the δf on the f_0 background. This, in turn, has been approximated by a Lorentz pitch-angle scattering operator in the calculations below, where the collision frequency for the species a is the sum of the deflection collision frequencies with all plasma species b (including like-particle collisions for which $a = b$), that is $\nu_a = \sum_b \nu_{ab}^{\mathrm{D}}$.

In a typical simulation the integration of the collisionless characteristics of each marker is then followed by a process simulating the pitch-angle scattering. This collisional step is carried out by assigning a random kick to the pitch-angle variable $\xi = \mathrm{atan}\left(v_\parallel / v_\perp\right)$. If the parallel and perpendicular velocity components of a given marker before the collision are dessignated $v_{\parallel \mathrm{in}}$ and $v_{\perp \mathrm{in}}$ respectively, and the initial value of the pitch-angle variable is $\xi_{\mathrm{in}} = \mathrm{atan}\left(v_{\parallel \mathrm{in}} / v_{\perp \mathrm{in}}\right)$, then following ξ becomes $\xi_{\mathrm{out}} = \left(\sin \Delta\vartheta \sin\varphi \sqrt{1 - \xi_{\mathrm{in}}^2} + \xi_{\mathrm{in}} \cos \Delta\vartheta \right)$, with $\Delta\vartheta = R\sqrt{2\nu \Delta t}$ [28, 29]. In the previous expression Δt is the time-step, ν the collision frequency as defined above, R a random number from a normal distribution function with expectation value zero and variance one and φ a random number from a uniform distribution between 0 and 2π.

Taking $f_0 = f_M \exp(-Ze\Phi_1/T)$, i.e. the solution of the zeroth order DKE,

$$\frac{\partial f_0}{\partial t} + \mathbf{v}_\parallel \cdot \nabla f_0 - \left(\mu \nabla_\parallel B + \frac{q}{m} \nabla_\parallel \Phi_1 \right) \frac{\partial f_0}{\partial v_\parallel} = C(f_0), \tag{15}$$

with $f_M = \left[n_0 / (2\pi)^{3/2} v_T^3 \right] \exp\left[-\left(v_\parallel^2 + v_\perp^2 \right) / 2 v_T^2 \right]$ the standard local Maxwellian, equation 10 becomes,

$$\frac{\partial f_1}{\partial t}+\dot{\mathbf{R}}\cdot\nabla f_1+\dot{v}_\parallel\frac{\partial f_1}{\partial v_\parallel}=-f_0\left(\mathbf{v}_\mathrm{d}+\mathbf{v}_{E1}\right)\cdot\nabla r\left[\frac{n'}{n}+\frac{q}{T}\Phi_0'+\left(\frac{mv^2}{2T}-\frac{3}{2}+\frac{q}{T}\Phi_1\right)\frac{T'}{T}\right]+C(f), \tag{16}$$

where the species index has been dropped for convenience, the prime denotes the derivative with respect to r, $\mathbf{v}_{E1}=\mathbf{b}\times\nabla\Phi_1/B$ is the $E\times B$ drift related to the potential variation, and the δf part has been relabelled as f_1. As we have pointed out, in 16 we are using equations (7)-(9) instead of 4-6. In particular, this implies the assumption that radially non-local terms, as well as terms involving the tangential components of the magnetic drift can be neglected when multiplying terms with f_1. The conditions that the magnetic configuration has to satisfy so that radially non-local terms can be dropped are identified in [23]. Neglecting the tangential components of the magnetic drift is correct as long as the $\mathbf{E}_0\times\mathbf{B}$ drift is sufficiently large. Finally note that in the present work f_0 differs from that in [20] where it is just f_M, i.e. Φ_1 is kept as a first order magnitude for all species, including the impurities, in that reference. This, which allows f_1 to develop the Boltzmann response, may be questionable when $Ze\Phi_1/T_Z$ becomes of order unity, and might lead f_1 to become not sufficiently smaller than f_0. In this sense the present ordering constraints more efficiently the smallness of f_1 and the neglected terms mentioned in the previous paragraph regardless of the value of Φ_1 and the impurity charge state.

The solution of equation 16 when Φ_1 is neglected leads to the same result as the standard mono-energetic and local neoclassical theory. In figure 1 a radial profile of the particle flux density for fully ionized carbon is presented, comparing results of EUTERPE and the 1D transport code NTSS [30, 31] which uses transport coefficients determined by DKES [32, 33]. Note that this benchmark case corresponds to the LHD magnetic configuration considered in section 3.1 for the case labelled as B.III and neglecting Φ_1 (see figures 3).

2.2. Solution of the quasi-neutrality equation in EUTERPE

Regarding the electric field calculation the ambipolar part Φ_0 is provided by the predictive transport code mentioned at the end of the previous section NTSS. This code uses precalculated DKES mono-energetic coefficient databases that are, given a set of equilibrium profiles, appropriately convoluted to obtain the particle fluxes necessary for the ambipolar root-finding [30]. For the calculation of Φ_1 performed with EUTERPE, instead of the less restrictive ambipolariy constraint the fulfilment of quasi-neutrality among all the species is considered,

$$\sum_a Z_a e n_a = 0. \tag{17}$$

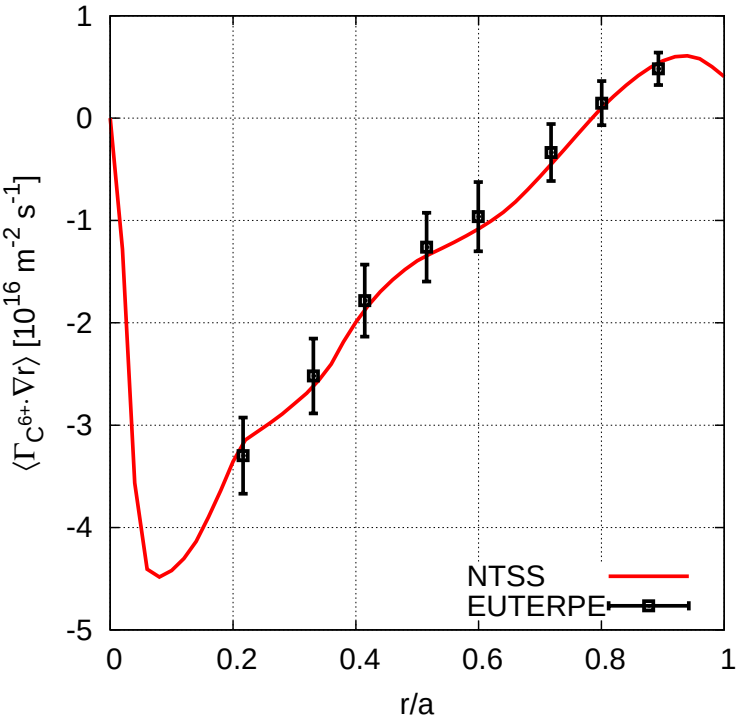

Figure 1: EUTERPE/NTSS comparison for the radial particle flux density of C^{6+} as a function of the normalised effective radius r/a. The plasma parameters correspond to the case B.III shown in figure 3 and $\Phi_1 = 0$ in this comparison.

Considering the density up to first order in ρ_* with the equilibrium part now varying on the flux surface due to the Boltzmann response

$$n_a = n_{0a} \exp(-Z_a e \Phi_1 / T_a) + n_{1a}, \tag{18}$$

and assuming that $\sum_a Z_a e n_{0a} = 0$, when electrons, bulk ions, and one single impurity species with charge Z are taken into account the following relation follows

$$\Phi_1 = \frac{T_e}{e} \left(n_{0e} + n_{0i} \frac{T_e}{T_i} + Z^2 n_{0Z} \frac{T_e}{T_Z} \right)^{-1} (n_{1i} - n_{1e} + Z n_{1Z}), \tag{19}$$

when the exponent of the Boltzmann factor is assumed much smaller than unity for all species. For the calculations carried out in this work the electron response is assumed to be adiabatic and f_{1e} is neglected since $f_{1e}/f_{1i} \sim \rho_{*e}/\rho_{*i}$ at comparable electron and bulk ion temperature. Since equation 19 is limited to the cases where $Ze\Phi_1/T_Z \ll 1$, and this limit is questionable in situations with moderate to high Φ_1 amplitude and Z, impurities then assumed in this work at a sufficiently low concentration so that their influence on the potential can be neglected. The leap in complexity if more terms in the series must be retained or the Boltzmann response was kept in its exponential form, leading to an equation non-linear in Φ_1, is beyond the scope of the present work. Thus, under these assumptions the equation for Φ_1 reduces to

$$\Phi_1 = \frac{T_e}{e}\left(n_{0e} + n_{0i}\frac{T_e}{T_i}\right)^{-1} n_{1i}, \tag{20}$$

and states that the potential to redress the lack of charge quasi-neutrality at this order is exclusively due to the first order departure of the bulk ion density from its equilibrium value.

When solving equation 20 a Fourier solver implemented in EUTERPE applies a low-mode-number filtering that defines the range of Fourier modes over which the equation is to be solved. In the present work poloidal and toroidal mode numbers m and n up to 4 have been sufficient to find good convergence of the calculated Φ_1 and the related impurity fluxes. EUTERPE calculates Φ_1 at each flux surface independently, which introduces a dependency on r since Φ_1 differs from one surface to another. Thus Φ_1 over the simulation time is better expressed as $\Phi_1(r, \theta, \phi, t)$. Here θ and ϕ are the angular-like magnetic (PEST [34]) coordinates. The poloidal drift due to the radial variation of Φ_1 will be ignored here since it is of the same magnitude as the tangential $\mathbf{b} \times \nabla B$ component of $\mathbf{v}_d$ ignored when simplifying equation 4 to equation 7. The time dependency is averaged out during the time interval where stationary values have been reached within numerical error. For the remainder of this paper we will write the dependence of Φ_1 as it is assumed and introduced as input for the impurity flux simulation: as a stationary potential $\Phi_1(\theta, \phi)$ which impurities do not influence given their low concentration. In figure 2 (left) an example of a Φ_1 contour plot is presented. The corresponding complex Fourier coefficients are shown separately for the real and imaginary parts and appear normalised to the component with maximum amplitude, which in this case is the $\cos\theta$ term. Again note that the representation of Φ_1 can be expressed as: $\Phi_1 = \sum_{m,n} [\Re(\Phi_{1,mn}) \cos(m\theta + n\phi) + \Im(\Phi_{1,mn}) \sin(m\theta + n\phi)]$. Finally the flux surface average $\langle \Phi_1 \rangle = \Phi_{1,00}$ must be zero since radial local trajectories are integrated. Nevertheless this is not strictly the case and $\Phi_{1,00}$ usually develops some small finite value during the simulation, which is due to the error accumulated in the numerical integration of the trajectories and the presence of a small radial numerical drift. A low amplitude of the component $\Phi_{1,00}$ indicates a weak numerical departure from the exact trajectories and is correlated to tolerable noise situations, and filtering it out does not impact appreciably the calculation of any other magnitude, including the radial flux of impurities. In figure 2 (right) such a situation is found where $\Phi_{1,00}$ finite but nevertheless small. These figures are obtained for the case B.III discussed later in section 3.1. A benchmark of the calculations of Φ_1 with the code SFINCS has recently been carried out and the results are presented in the appendix.

3. Radial flux of impurities including Φ_1

In this section the numerical results are presented and discussed. Three different stellarator configurations, each from a different device type, have been considered: the Large Helical Device (LHD, Toki, Japan) heliotron; the Wendelstein 7-X (W7-

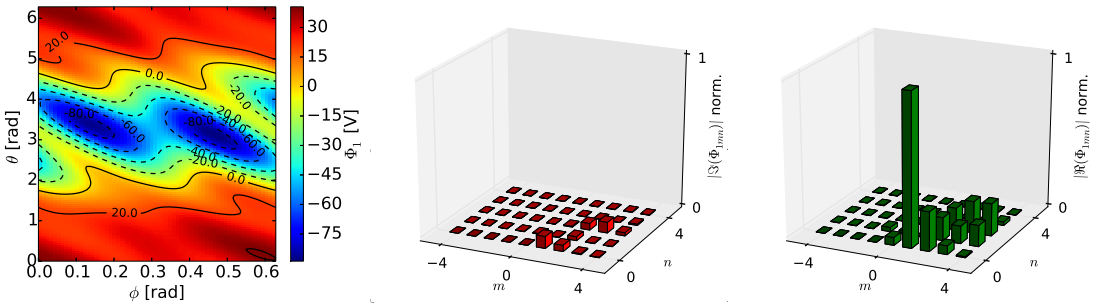

Figure 2: (Left) Stationary Φ_1 obtained with EUTERPE as a function of the poloidal and toroidal coordinates θ and ϕ. Absolute values of the real and imaginary parts (center and right figures respectively) of the Fourier coefficients $\Phi_{1,mn}$ normalized to the modulus of the largest component, in this case $\cos\theta$.

Magnetic configurations			
Device	$B_{00}(r/a = 0.5)$ [T]	R_0 [m]	a [a]
LHD	1.54	3.6577	0.5909
Wendelstein 7-X	2.78	5.5118	0.5129
TJ-II	0.996	1.5041	0.1926

Table 1: Major and minor radii, R_0 and a respectively, and amplitude of the Boozer harmonic B_{00} of the magnetic field at the mid plasma radius of the three studied configurations.

X, Greifswald, Germany) helias; and the TJ-II (Madrid, Spain) heliac. For each device a vacuum configuration has been considered and the radial particle flux of some representative impurities calculated, comparing the result when Φ_1 is neglected to the result when Φ_1 is retained. The scanned plasma parameters have resulted in 6 different pairs of density and temperature profiles for LHD, 5 for W7-X and 2 for TJ-II. The main parameters related to the three magnetic configurations taken into account are provided in table 1.

3.1. LHD results

For LHD two different density profiles have been considered: one corresponding to a high-density scenario and one corresponding to a low-density scenario. Following the contour plot of the magnetic field modulus at $r/a = 0.6$ presented in 3 (left), the second plot from the left shows the two density profiles, and are labelled respectively as A for the high electron density n_{0e}, and B for the low n_{0e}. For each set of profiles considered throughout this work a three species plasma has been assumed (hydrogen as bulk ions, electrons and one impurity species with charge Z). For the LHD results presented in this section fully ionised carbon C^{6+} and neon Ne^{10+} have been considered.

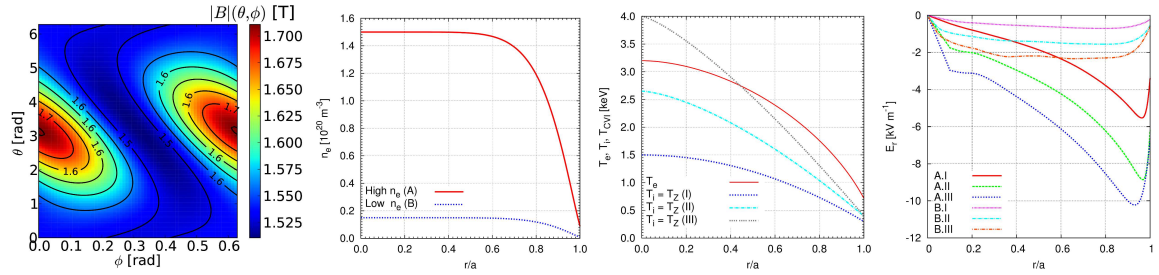

Figure 3: From left to right: magnetic field strength of the LHD equilibrium used at the radial position $r/a = 0.6$; electron high-density (A) and low-density (B) radial profiles; electron, hydrogen and impurity temperature radial profiles considered; ambipolar electric field E_r profiles of the six resulting pairs of ion density/temperature profiles.

The equilibrium density of the bulk ions n_{0i} and impurities n_{0Z} is then initially taken so that quasi-neutrality among all the species at zeroth order is fulfilled. Thus $n_{0Z}(r) = n_{0e}(r)\,[Z_{\text{eff}}(r) - 1]\,/\,[Z(Z-1)]$ and $n_{0i}(r) = n_{0e}(r)\,[Z - Z_{\text{eff}}(r)]\,/\,(Z-1)$. The reference value considered for the effective charge is taken in all cases to be $Z_{\text{eff}} = 1.1$ and it is held constant over r, which results in the bulk and impurity ion density profiles having the same shape as the electron density profile. The temperature profile of the impurities and bulk ions, taken equal, has been scanned, keeping the electron temperature profile fixed. These profiles sorted in increasing order of ion temperature are labelled as I, II and III and are shown in figure 3 (third plot from the left). Finally the ambipolar electric field E_r provided by NTSS is presented in the rightmost plot. Note that for all the LHD plasmas presented here E_r is negative, and for the low-collisionality cases B, E_r is relatively close to zero. The corresponding impurity inward pinch is then smaller than at higher collisionalities, which should make it easier for higher-order corrections to counteract the inward impurity pinch [35] as is shown below. In figure 4 the normalised electrostatic potential $e\Phi_1(\theta,\phi)/T_i$ is presented for the three aforementioned ion temperature profiles I, II and III at the radial position $r/a = 0.6$. The three figures on the top correspond to the high-density cases A.I-III while the plots on the bottom corresponds to the low density B.I-III cases. As the collisionality decreases and the temperature increases (i.e. following the six contour plots from left to right and top to bottom) the normalised potential increases up to one order of magnitude from case A.I to B.III. Considering that Φ_1 scales with the ion temperature (see equation 20) and that the collisions prevent the localised particles from completing their orbit and effectively contributing to Φ_1, the trend that $e\Phi_1/T_i$ follows is qualitatively as expected.

Figure 5 shows the real and imaginary part of some Fourier coefficients of Φ_1 with representative poloidal and toroidal mode numbers. The typical values of the largest terms vary from a few volts of peak-to-peak potential variation in case A.I to around a hundred in case B.III. The change in the spectrum of the potential between the high density cases

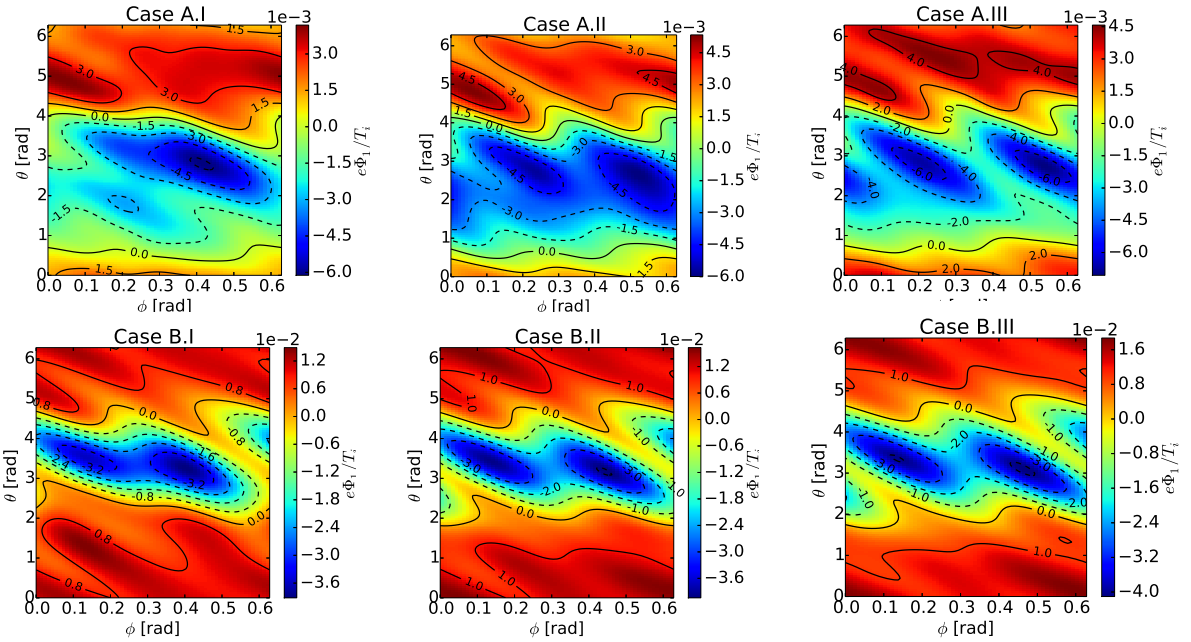

Figure 4: At the position $r/a = 0.6$ for LHD: on the top row $\Phi_1(\theta, \phi)$ for the high-density profile cases A and on the bottom row for the low-density cases B.

and the low density cases is appreciable too. At high density (top figures) the spectrum consists basically of two large $\sin\theta$ and $\cos\theta$ components of comparable size followed by other components appreciably lower in absolute value, among which the $\cos 2\theta$ is the largest. On the other hand, the spectrum of Φ_1 for the low-density cases (bottom figures) is characterised by a dominant $\cos\theta$ component with no other component of similar prominence. In order to sketch what underlies these changes in the spectrum note first that Φ_1, under the assumptions considered, reflects the same dependence as that of n_{1i} (see equation 20), given by the perturbed distribution function of the bulk ions f_{1i}. Regarding the dependence of the latter, and in particular the portion related to the ripple-localised particles which are largely responsible for Φ_1, it is known for a classical stellarator [15, 36] that in the asymptotic limit where the effective collision frequency exceeds the $E_r \times B$ poloidal precession frequency ($\Omega_E = E_r/rB_0 \ll \nu_i$) the distribution function consists essentially of a $\sin\theta$ component, while in the opposite *rotational limit* ($\Omega_E \gg \nu_i$) this becomes to a good approximation a $\cos\theta$ term. In the cases presented, the parameters are such that Ω_E/ν_i take values from approximately 0.2 for the simulation with the highest ion collisionality (case A.I at $r/a = 0.8$) to 20 at the lowest collisional one (case B.III at $r/a = 0.8$). Thus qualitatively the changes in the Fourier spectrum of Φ_1 can be reasonably well explained.

The question to what extent the radial impurity transport is affected by Φ_1 has been addressed considering the potential calculated at four different radial positions for each set of profiles: $r/a = \{0.2, 0.4, 0.6, 0.8\}$. The calculated potential at a given flux surface

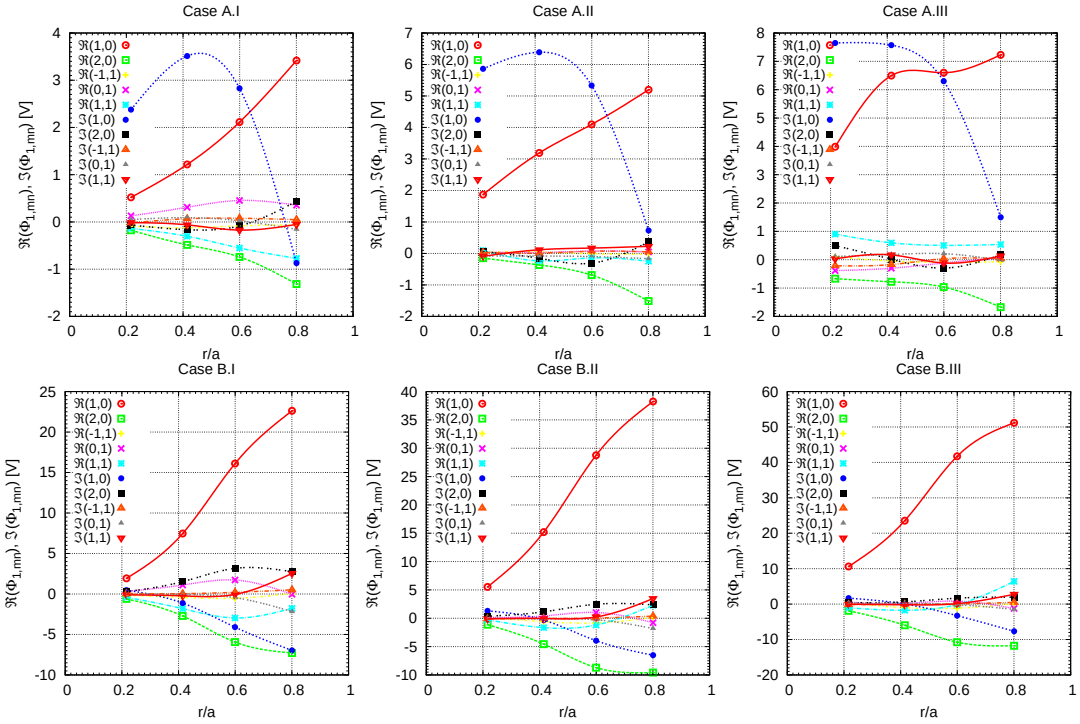

Figure 5: Real and imaginary parts of the Fourier harmonics of Φ_1 as a function of r/a for the six LHD cases considered.

has been taken as an input for the estimation of the radial particle flux density $\langle \mathbf{\Gamma} \cdot \nabla r \rangle$ of the impurity of interest. In figure 6 the results for LHD are shown. In all plots filled/open points correspond to the result including/neglecting Φ_1. For better visualisation, points are connected by a solid/dashed curve respectively. The impurity species is denoted by a different point type and line colour. Fully ionised carbon and neon, C^{6+} and Ne^{10+}, are represented with black circles and green diamonds respectively. The radial particle flux density is represented normalised to the equilibrium density value n_{0Z} at each position. The electron density profile (A or B) and impurity temperature case (I, II or III) are indicated in the legend.

In a first overview of figure 6 and looking at the corresponding contour plots with the ratio $e\Phi_1/T_i$ shown in figure 4, for the two impurity species, a more significant change in the impurity fluxes is observed with increasing $e\Phi_1/T_i$.
Focusing on the high-density cases A, for the two impurity species the effect of the potential variation is initially found to be weak, see case A.I, and becomes more appreciable as the amplitude of $e\Phi_1/T_i$ amplitude (and the ion temperature) increases, see cases A.II and A.III. A large impact on the shape of the impurity flux profiles is not observed but mitigation of the inward flow does occur in the three cases for both carbon and neon.
We observe that for the low density cases B for the three species Φ_1 has a much stronger

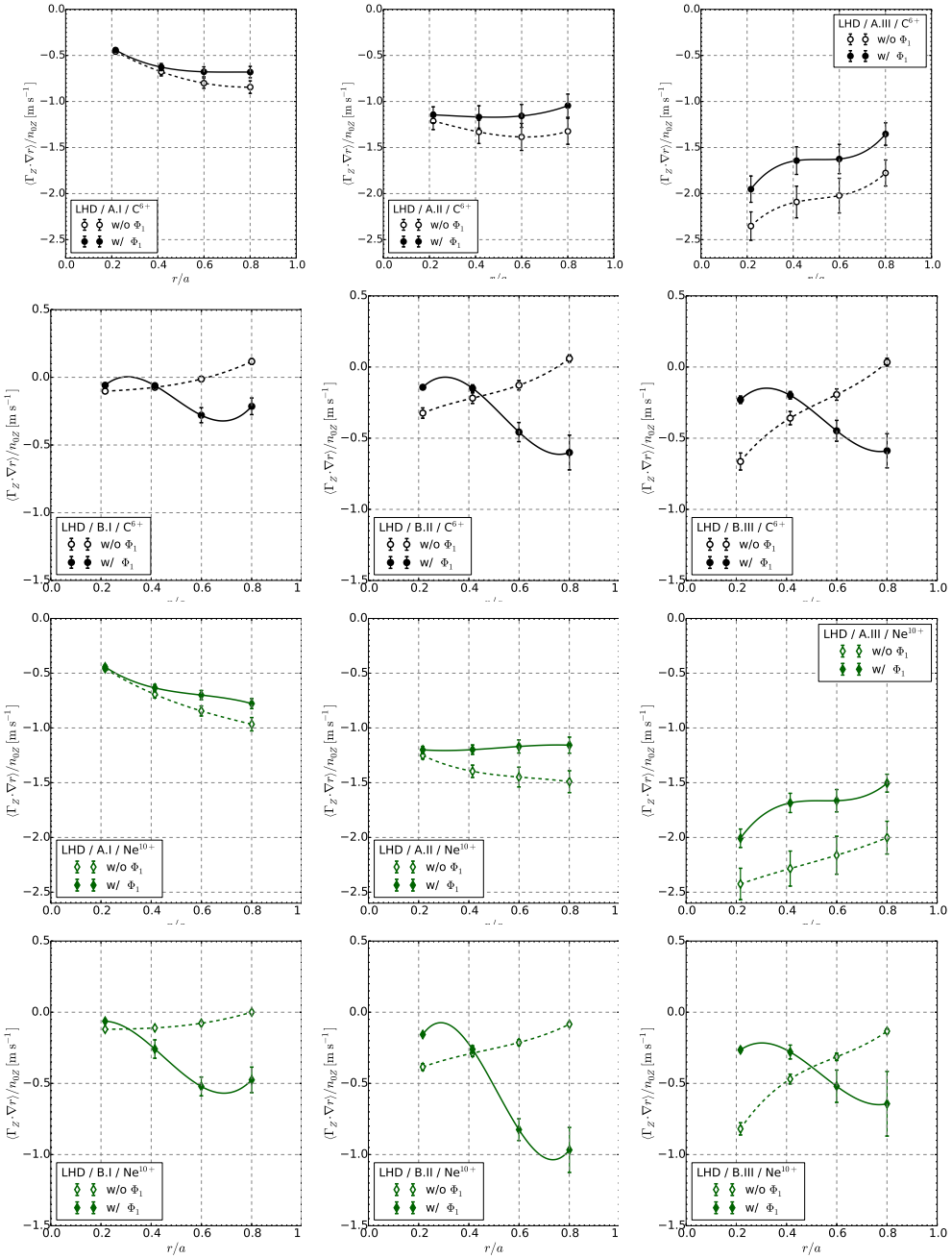

Figure 6: Radial particle flux density $\langle \mathbf{\Gamma} \cdot \nabla r \rangle$ normalised to the equilibrium density n_{0Z} for C^{6+} (circles), Ne^{10+} (diamonds) including Φ_1 (filled points linked by solid lines) and neglecting it (open points linked by dashed lines). For visualisation purposes points are linked with cubic splines fitting curves.

impact on the radial flux than at high densities. Not only in absolute value but also in overall trend along the radial coordinate. Apart from the larger $e\Phi_1/T_i$ values the *background plasma* should not be overlooked [35]. For the low collisionality cases B the standard inward impurity pinch is smaller, and the correction caused by Φ_1 makes a

larger difference of the total impurity flux than in the cases without. Without Φ_1 and regardless of the temperature profile (I, II or III) the radial flux of carbon monotonically becomes less negative with increasing r. The effect of Φ_1 reverses that tendency, leading to a stronger inward flow at the outer radii and a weaker one at the more inner positions. This loss of *similarity* between radial profiles with and without Φ_1 is significantly more evident as Φ_1 increases. Regarding the impact of the charge state, neon exhibits a slightly more pronounced change when Φ_1 is considered than carbon does.

The underlying reasons that make the effect of Φ_1 mitigating or supporting the tendency to accumulate impurities, are difficult to deduce when comparing across cases and radial positions. The results indicate the necessity of a deeper quantitative look into the the problem, beyond the mere correlation between parameters discussed so far, namely, potential amplitude, collisionality, charge state, etc.
To outline the intricate coupling that leads Φ_1 to produce net particle transport note first that contrary to the magnetic field modulus B, Φ_1 does not preserve the stellarator symmetry as it contains both cosine and sine components. This lack of stellarator symmetry arises indeed from the stellarator symmetry of B, that introduces only sine terms in the transport source $\mathbf{v}_d \cdot \nabla r$, which coupled to the cosine terms of f_1 vanish when the flux surface average operates on the particle-flux-density integral. Thus, the physical situation with non-zero radial transport requires f_1 to have sine components that, as discussed above, are the same for n_{1i} and Φ_1. As a consequence, when Φ_1 is taken into account and together with it $\mathbf{v}_{E1} \cdot \nabla r$ as a transport source for the impurities, it is straightforward to recognise that this can drive radial transport through both sine and cosine terms of Φ_1 coupled respectively to the cosine and sine components of f_1. Then, returning to the question of how a particular Φ_1 affects on counteracting the inward flux of impurities depends on the spatial dependence of f_{1Z}, or equivalently, the answer requires to know how the perturbed impurity density n_{1Z} on the flux surface varies. To illustrate this coupling figure 7 shows an example of how the perturbed density and cross field drifts change from the situation without Φ_1 to the one that includes it. The figure refers to the carbon B.III case at the innermost radial position $r/a = 0.2$ (see bottom right plot in figure 6), which shows a reduction of the inward flux when Φ_1 is present. The radial drifts for the two cases, magnetic $\mathbf{v}_d \cdot \nabla r$ (top left) and the sum of magnetic and electrostatic $(\mathbf{v}_d + \mathbf{v}_{E1}) \cdot \nabla r$ (top right), are presented. For this example the thermal energy equally divided among the parallel and perpendicular kinetic energy has been considered for the drifts shown.
In the two bottom plots the density variation of carbon $n_{1C^{6+}}$ are represented for the case without Φ_1 (bottom left) and for the case with Φ_1 (bottom right). The contours of the radial drifts of the top figures are superimposed to the corresponding density contour plot for visualisation purposes. In the first of the density contour plots one can observe that the density exhibits an up-down pattern with low (high) density values around $\theta = \pi/2$ ($\theta = 3\pi/2$). The low density areas of the flux surface appear predominantly encompassed by contours of strong positive radial drifts while the high density regions

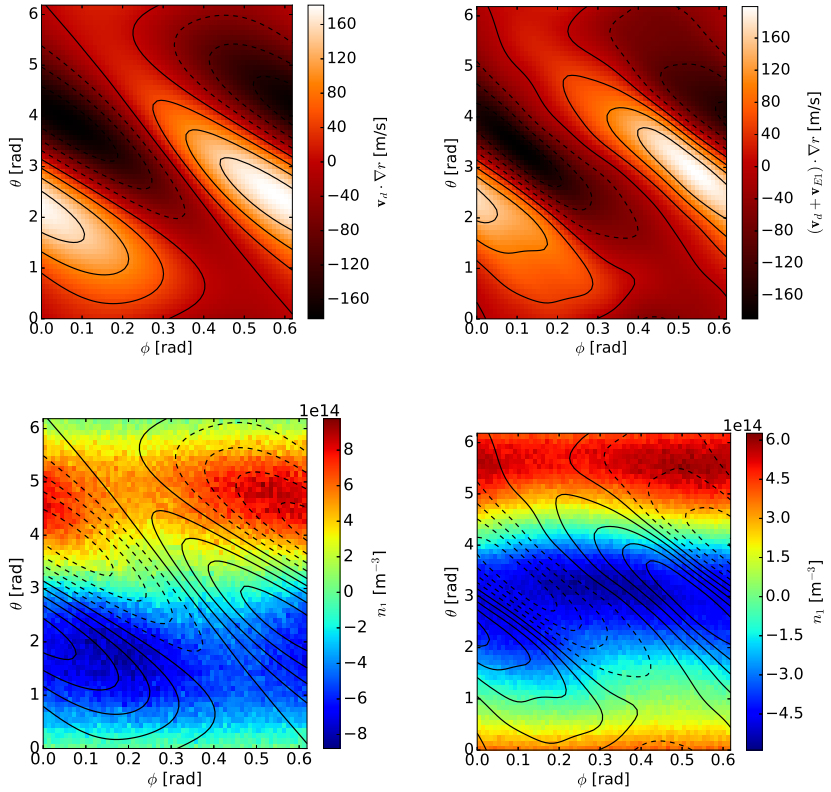

Figure 7: For the B.III LHD case at the radial position $r/a = 0.2$ (see figure 6): radial magnetic drift across the flux surface $\mathbf{v}_d \cdot \nabla r$ (top left); sum of the magnetic and $\mathbf{E}_1 \times \mathbf{B}$ drifts across the flux surface, $(\mathbf{v}_d + \mathbf{v}_{E1}) \cdot \nabla r$ (top right); first order departure of the carbon density $n_{1C^{6+}}$ when Φ_1 is neglected together with the contours of $\mathbf{v}_d \cdot \nabla r$ (bottom left); $n_{1C^{6+}}$ when Φ_1 is taken into account together with the contours of the $\mathbf{v}_d \cdot \nabla r$ (bottom right). In the bottom figures dashed/solid contours correspond to radially inward/outward drifts.

coincide with those of negative drifts. This situation, that clearly supports the inward flow of carbon ions, is lost when Φ_1 is present. In that case (see bottom right plot) a *phase shift* of $\pi/3 - \pi/2$ along θ in the carbon density, which becomes in-out asymmetric instead, leads the radial drift contour of largest outward and inward values to be both situated in the low density region located in between $\theta = \pi/2$ and $3\pi/2$. This does not support the enhancement of the inward pinch as was the case without Φ_1.

3.2. Wendelstein 7-X results

In this section similar numerical simulations to those discussed in the previous one for LHD are presented for the stellarator Wendelstein 7-X (W7-X). We consider a similar scan of the ion temperature profiles, set equal to the temperature of the impurity, as shown in figure 8. From left to right the four plots represent: the magnetic field mod-

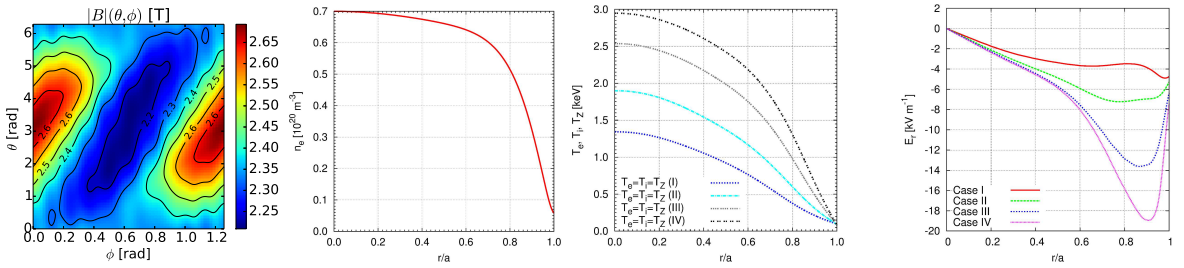

Figure 8: From left to right: magnetic field strength in one W7-X period at the position $r/a = 0.6$; electron density radial profile; scanned temperature profile, taken to be equal hor electrons, hydrogen ions and impurities; ambipolar electric field E_r profiles for each case.

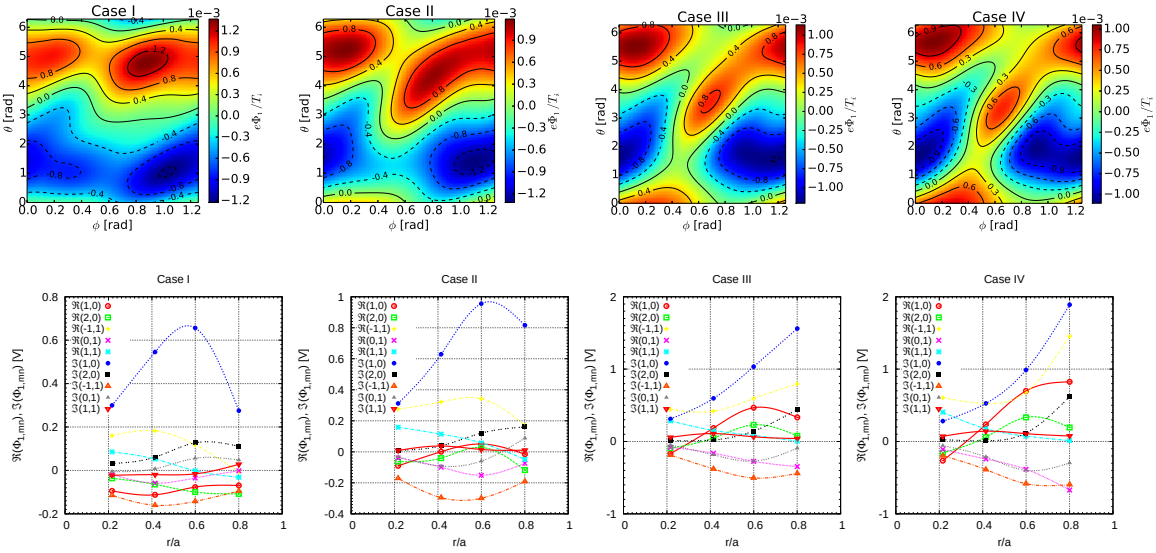

Figure 9: On the top row: Φ_1 contour plots at the radial position $r/a = 0.6$ for the W7-X cases I, II, III and IV (from left to right). On the bottom row: real and imaginary part of some Fourier harmonics of Φ_1 as a function of r/a each case.

ulus in one W7-X period at $r/a = 0.6$; the electron density n_{0e} (as before, an effective charge $Z_{\text{eff}} = 1.1$ taken independent of r defines the bulk and impurity ion density radial profiles); the four different $T_i = T_Z$ radial profiles which are labelled as I, II, III and IV increasingly with T; and the ambipolar radial electric field obtained with NTSS.

The top row of figure 9 shows contour plots of the normalised electrostatic potential $e\Phi_1/T_i$ varying over the surface at the radial position $r/a = 0.6$. The values of $e\Phi_1/T_i$ calculated for W7-X are appreciably lower than for the LHD cases at comparable collisionality, which corresponds roughly to the high density cases A.I-III in figure 4 (top row) (a comparison of all simulation results is given in figure 17). The reason for

the low value of the electrostatic potential in W7-X is the aim of the design of this device namely, reducing the neoclassical losses and bootstrap current by approaching an omnigeneous magnetic field structure. In a perfectly omnigeneous magnetic field the bounce-averaged drift surfaces of the localised particles coincide with the flux surfaces. Although this ideal situation cannot be exactly reached [37], the W7-X magnetic field structure is a better approximation than the other devices considered in this work, leading to a smaller departure of the localised particles from the flux surfaces and resulting in a weaker electrostatic potential variation on them. Regarding the Fourier spectrum of Φ_1, similar features to LHD at comparable collisionality (cases A.I-III) are seen. A dominant $\sin\theta$ component and a weaker $\cos\theta$ that grows as collisionality decreases appear in both the W7-X and the LHD cases. On the other hand, the W7-X potential exhibits a broader spectrum, in the sense that the rest of the components are not as small – especially at the outer radii – as in LHD, where with the exception of $\cos 2\theta$ the remaining Fourier harmonics cluster around the value zero.

In figure 10 the particle flux density calculated for fully ionised carbon C^{6+} (circles) and Tungsten W^{40+} (triangles) is presented for the four ion temperature profiles in the top and bottom rows respectively. As before, filled (open) points linked with solid (dashed) lines correspond to the calculation including (neglecting) the potential variation on the surface. Looking at the carbon cases, the difference that Φ_1 makes with respect to the standard neoclassical prediction is difficult to discern for the lowest temperature cases like I or II. As the ion temperature increases, in III and IV for instance, the impact becomes distinguishable and results in a weak mitigation of the inward radial flux. Nonetheless Φ_1 makes little difference in the flux levels of these cases too. In the comparison for tungsten impurities shown on the bottom row of figure 10 the trend is the same, although the larger charge state makes the difference more clear between taking into account the potential variation and neglecting it, particularly in the lowest collisional cases III and IV.

As mentioned in the previous paragraph, none of the cases presented so far for W7-X is comparable in parameters and collisionality to the LHD low density cases B, which were the cases that showed the most significant quantitative and qualitative change so far due to Φ_1. Thus, in order to allow a comparison with those LHD cases an additional set of profiles for W7-X is presented. It corresponds to a W7-X plasma with off-axis ECRH where the density is lower than in the previous cases and the electron and ion temperature are comparable to the previous case IV. The profiles are shown in the left and central plots of figure 11 and the ambipolar radial electric field on the right. The sample of Φ_1 at the position $r/a = 0.6$ is presented in figure 12 (left) and the main Fourier harmonics of Φ_1 are plotted in figure 12 (right) as a function of r/a. In this case the maximum potential amplitude is twice as high as in the previous case IV. The spectrum exhibits a very distinctive dependency along r, where no clear dominance of any component is present, except at the outer-most position where the components $\sin(\phi - \theta)$ and the $\sin\phi$ are larger than the remaining ones in absolute value.

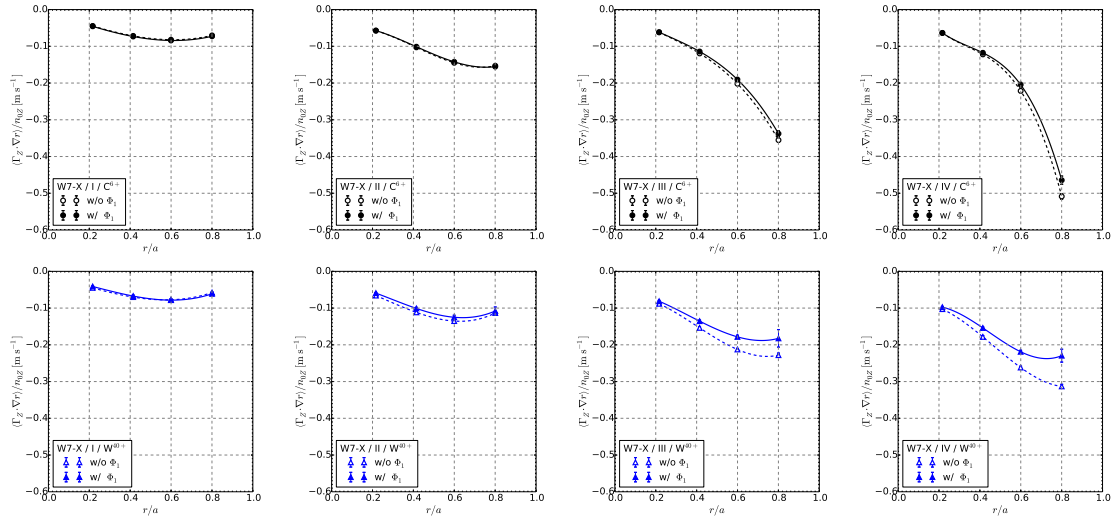

Figure 10: Radial flux density of C^{6+} (top) and W^{40+} (bottom) as a function of r/a including Φ_1 (solid line) and neglecting it (dotted line). The cases I to IV are displayed from left to right.

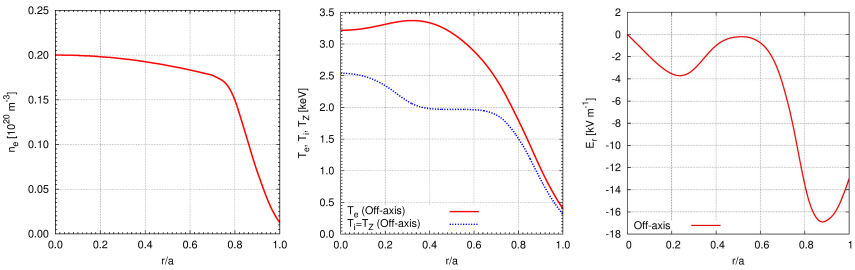

Figure 11: For the W7-X case with off-axis ECRH, from left to right: electron density radial profile; temperature radial profiles for hydrogen ions, electrons and impurities; ambipolar electric field E_r.

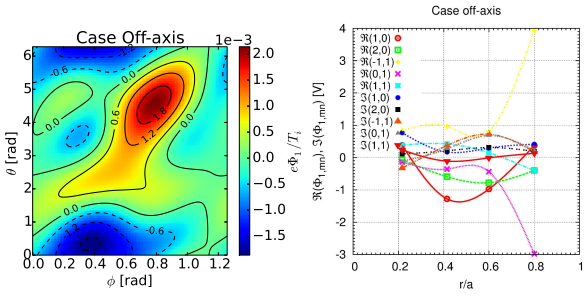

Figure 12: Electrostatic potential variation at $r/a = 0.6$ and some representative Fourier harmonics of Φ_1 as a function of r/a for the W7-X case with off-axis ECRH.

Regarding the impurity radial fluxes, in the case of carbon (figure 13 left) the correction introduced by Φ_1 is practically negligible. It is necessary to increase substantially the

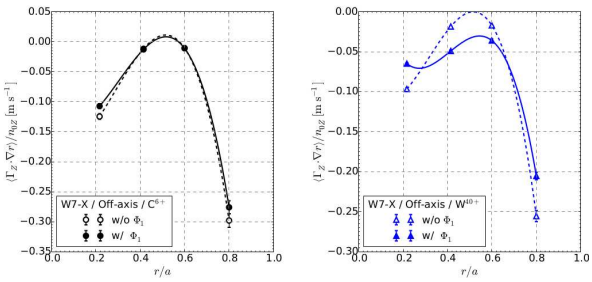

Figure 13: Radial particle flux density of C^{6+} (left) and W^{40+} (right) as a function of r/a including Φ_1 (filled dots linked with solid line) and neglecting it (open dots linked with dashed line) for the W7-X case with off-axis ECRH..

charge state, (see figure 13 right for a similar comparison for W^{40+}) to notice the difference. Here the inward pinch without Φ_1 is barely zero ($r/a = 0.2$ and 0.4), due to the low negative E_r values (see figure 11 right). And the introduction of Φ_1 leads the inward pinch to become appreciable. Anyhow, the difference between the case without and with Φ_1 is still not larger than in case IV discussed above, despite of the stronger $e\Phi_1/T_i$ in a factor 2. This lack of response to a larger $e\Phi_1/T_i$ may indicate again that the specific coupling between the potential variation and the distributing function density f_{1Z} is playing a role, as the discussion at the end of section 3.1 is noted. This represents an entire topic to look deeper into in another work.

3.3. TJ-II results

Finally in the present section two cases are considered for the TJ-II stellarator. A contour plot of the magnetic field modulus of the configuration considered at the radial position $r/a = 0.6$ is shown in figure 14 (left). Two electron density profiles (high and low density) shown in figure 14 (second plot from the left) have been taken into account, with the temperature profiles for the electrons, bulk ions and impurities given in figure 14 (third plot from the left). The corresponding two ambipolar electric field profiles are shown in figure 14 (right). The impurities considered are fully ionised carbon C^{6+} and partly ionised tungsten W^{15+}. These profiles correspond to typical NBI-heated TJ-II plasmas [38, 39].

In figure 15 (top) the normalised electrostatic potential $e\Phi_1/T_i$ is plotted at the radial position $r/a = 0.6$ for the high- and low-density cases. The amplitude of some representative Fourier harmonics (bottom) are also shown. Looking at the latter figure the harmonics of Φ_1 are lower in amplitude than LHD and of the same order of magnitude as in the W7-X cases, of a few volts. Nevertheless, the much lower ion temperature of these TJ-II examples indeed represents the largest ratio $e\Phi_1/T_i$ at comparable collisionality of the three devices studied – see figure 4 (top) and 9 (top) for the same magnitude represented for LHD and W7-X similar collisionality cases –. Further discussion comparing all the cases studied in this work is provided in section 4,

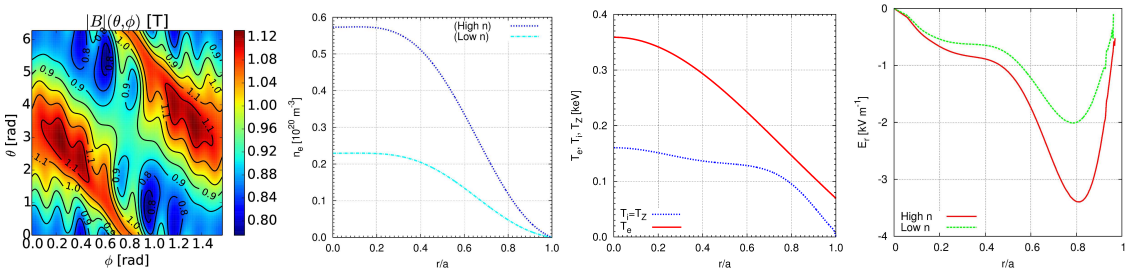

Figure 14: From left to right: magnetic field strength in one TJ-II period at the position $r/a = 0.6$; electron high and low density radial profiles of a typical NBI-heated plasma; electron, hydrogen and impurity radial temperature profiles; ambipolar electric field E_r profile for the two cases considered.

but we note already in this section that the electrostatic potential energy related to Φ_1 can vary up to 5-8 % in terms of thermal energy for the high density TJ-II case and up to 10-15 % for the low density one. For LHD and W7-X the variation is respectively one and two orders of magnitude lower than that. In contrast to W7-X, where the neoclassical optimisation undergone for its design underlies the weak Φ_1, the lack of such optimisation in TJ-II and much larger effective ripple (see Ref. [9]) supports large potential variations like those calculated here and observed experimentally [40].
The results for the radial impurity flux are represented in figure 16 for the high/low density cases in the two figures on the left/right, and for the two species considered, C^{6+} on top and W^{15+} on the bottom. The radial impurity transport is not affected by the presence of Φ_1 to the extent its large amplitude for such low temperatures might lead one to expect. It does not differ qualitatively from the standard neoclassical prediction, although quantitatively the changes observed in the flux are appreciable and tend to decrease the inward flux. The difference on the impact for carbon and tungsten are also of comparable order of magnitude regardless of the different charge states. This weak response to relatively large values of Φ_1 and charge state again points out to the fact that the impact of Φ_1 on the radial transport cannot be explained only with the magnitude of the parameters under discussion. As noted at the end of section 3.2 and more in detail in section 3.1, the spatial dependence of f_{1Z} depends on these parameters too and changes from case to case, and with it, the coupling with Φ_1 to finally impact the radial transport more or less efficiently. Finally, regarding the spectrum of Φ_1 shown in figure 15 (bottom), TJ-II exhibits several large terms, among which the $\cos\theta$ is the largest along r for both density cases. Not much smaller are also found others like the $\sin\theta$, the helical components $\cos(\theta+\phi)$ or $\sin(\theta+\phi)$.

4. Final remark on the amplitude of Φ_1 in LHD, W7-X and TJ-II

The smallness of $Ze\Phi_1/T$, as was noted in the introduction, indicates the reliability of the standard neoclassical neglect of Φ_1 as source of trapping and radial transport

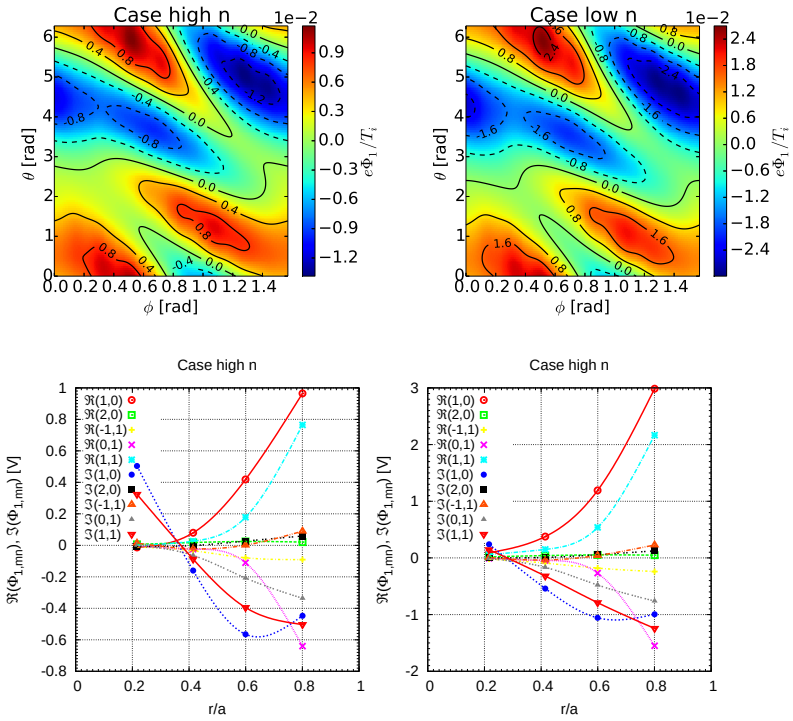

Figure 15: At the position $r/a = 0.6$ for TJ-II standard configuration: Φ_1 contour plots for the high and low density TJ-II cases (top) together with the corresponding radial profiles of some selected Fourier components (bottom).

of impurities compared to the magnetic field gradient and curvature. Taking $\Delta\Phi_1$ to be the maximum potential variation on a flux surface, $e\Delta\Phi_1$ is subsequently the total energy variation that a bulk ion, or impurity if multiplied by Z, can experience on a flux surface due to Φ_1. In order to compare all the cases and configurations considered here, figure 17 shows the ratio $e\Delta\Phi_1/T$ as a function of the bulk ion normalised to the bounce frequency, $\nu^* = \nu_{i,T}R/v_{Ti}\iota$ where ι is the rotational transform. The figure takes into account the four radial locations considered for each set of profiles and devices considered in the present paper.

Observing this representation it is clear that assuming mono-energetic trajectories for impurities easily becomes questionable and the effect of Φ_1 (as confirmed in the simulations presented) can be important in LHD and TJ-II. In these two devices the electrostatic energy variation normalised by the thermal energy exceeds at most radial positions and in most cases the level of a few percent (and in some cases ten percent). This ratio appropriately scaled by a moderate to large impurity charge (and at some positions also by a low charge) becomes of order unity. This is clearly the case for the low-density set of LHD profiles B.I-III and the two TJ-II cases. TJ-II exhibits potential variations of the order of those given in LHD at the much lower collisional set of profiles B. At a comparable range in collisionality, LHD cases A.I-III develop a Φ_1 roughly an order of magnitude lower than TJ-II. Similarly, comparing W7-X and LHD, the former

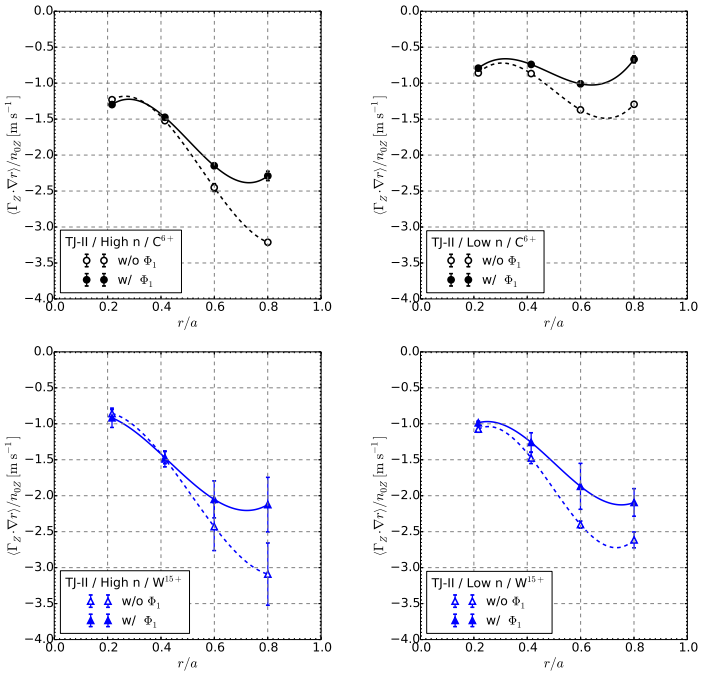

Figure 16: Radial particle flux density of C^{6+} (top) and W^{15+} (bottom) as a function of r/a including Φ_1 (filled dots liked by solid lines) and neglecting it (open dots linked by dashed lines), for the high and low density TJ-II cases (left and right respectively).

device has values of $e\Delta\Phi_1/T$ one order of magnitude lower than comparable cases for the latter.

For the W7-X cases studied, the ratio on the other hand takes maximum values of around and slightly below one percent, which may result in a moderate impact on highly charged impurities like the tungsten, but has a negligible effect on the radial transport of low charge impurities like carbon.

Finally, the quantitative impact of Φ_1 and the conclusions drawn from the cases considered in this work should be taken cautiously when extrapolating them to parameters distant from the present ones, as they follow from a limited set of profiles. In addition, the changes in the impurity distribution function f_{1Z}, and hence in the density of impurities n_{1Z}, are noted to play a role from the fact that in a few examples the impact is weaker than what could be expected from the considered parameters.

5. Summary and conclusions

The radial transport of impurities is known to be strongly influenced by the ambipolar part of the electrostatic potential, usually considered as an approximation to the full neoclassical electrostatic potential. In the present work, we have also taken into account the potential variation on the flux surface Φ_1 after solving the quasi-neutrality equation. The impact of Φ_1 on the radial particle flux of a few impurity species in the devices

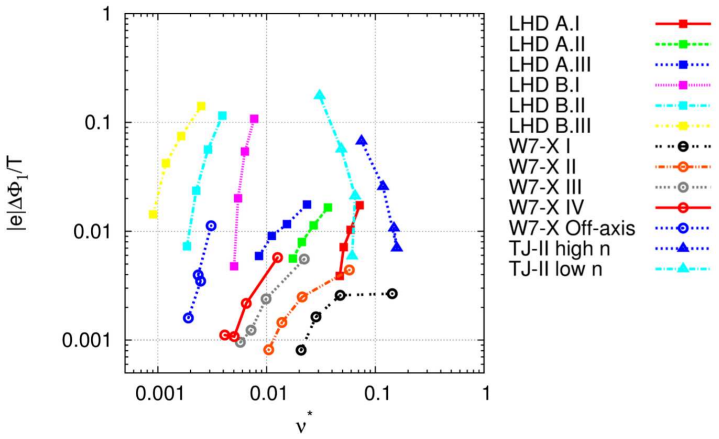

Figure 17: Normalized maximum variation of the potential $e\Delta\Phi_1/T_i$ for all the cases presented in this work, as a function of the normalised thermal collision frequency ν^*.

LHD, W7-X and TJ-II, using the code EUTERPE has been presented considering some typical plasma profiles.
The calculations have to a varied extent confirmed the importance of taking Φ_1 into account to quantitatively assess the radial transport of impurities. In LHD the effect of Φ_1 was visible in all cases, and in the low collisional ones strong corrections in the radial flux profiles have been shown, including both the mitigation and enhancement of the inward flux. In typical TJ-II NBI-heated plasmas including the role of Φ_1 has resulted in appreciable changes as well, although weaker than what could be expected from the large potential variation predicted for this device.
Finally, in W7-X $e\Phi_1/T$ has been found roughly to be one order of magnitude lower than in LHD and nearly two orders below TJ-II. Low charge impurities like C^{6+} are thus unaffected by Φ_1 but highly charged impurities like W^{40+} could experience some moderate change in their fluxes.

Apart from a more exhaustive parameter and magnetic configuration scan, some issues remain open, namely: study of the specific coupling between n_{1z} and Φ_1 which may result in scenarios of efficient mitigation of the tendency to impurity accumulation; the relaxation of the tracer impurity limit since accumulation unavoidably leads to appreciable impurity concentrations; relaxation of the assumption of an electron adiabatic response whenever meaningful.

6. Acknowledgements

This work has been carried out within the framework of the EUROfusion Consortium and has received funding from the Euratom research and training programme 2014-2018 under grant agreement No 633053. The views and opinions expressed herein do not necessarily reflect those of the European Commission.

The calculations were carried out using the HELIOS supercomputer system at Computational Simulation Centre of International Fusion Energy Research Centre (IFERC-CSC), Aomori, Japan, under the Broader Approach collaboration between Euratom and Japan, implemented by Fusion for Energy and the JAEA.
Some simulations have been performed on the local cluster in Greifswald, support of Henry Leyh and Matthias Borchardt is appreciated. The authours would like to thank Dr. I. Calvo (Ciemat) for helpful discussions.

Appendix A: Benchmark between EUTERPE and SFINCS

SFINCS [41, 22, 42, 43, 44] is a 4D drift-kinetic equation solver for computing radially local neoclassical phenomena in non-axisymmetric plasmas. The code can be run with an arbitrary number of kinetic plasma species, and it implements the full linearized Fokker-Planck-Landau operator for self- and inter-species collisions. Numerically, it uses continuum methods, with finite differences in the two spatial coordinates (poloidal and toroidal angles θ and ϕ), and spectral methods in the two velocity coordinates (normalized speed $x = v/v_{th}$ and pitch-angle $\xi = v_{\|}/v$). SFINCS has recently been updated to account for the flux-surface variation of the electrostatic potential, solving a system that is nonlinear in the unknowns, f_1 and Φ_1. The system that is solved includes the drift-kinetic equation, the quasi-neutrality equation, and a set of additional constraints for the unknowns. These constraints have been added, in conjunction with introducing particle and heat sources in the drift-kinetic equation, to enable a steady-state solution to exist (see refs. [41, 22] and for additional details).

In the present work we use the same quasi-neutrality equation in SFINCS as in EUTERPE, i.e. the electrons are assumed adiabatic and impurities are neglected, and we do our calculations with the pitch-angle scattering operator. However, it should be noted that there are three differences compared to the EUTERPE implementation: Firstly, even though the impurities are neglected in the quasi-neutrality condition the whole system is still solved simultaneously which implies that it is still nonlinear (i.e. Φ_1 is not given as a direct input to the kinetic equation of the impurities). Secondly, in the kinetic equations of both the main ions and the impurities SFINCS neglects collisions with the adiabatic electrons. And third in SFINCS there is no Fourier-filtering of $\Phi 1$, that is, Φ_1 is stored with the same θ and ϕ resolution as f_1. The numerical resolution which is required for convergence in SFINCS depends strongly on the magnetic geometry and the collisionality. In the long mean-free-path regime the number of grid points required in θ, ϕ and ξ can increase dramatically as the collisionality decreases. Since the time and memory requirements increase significantly when more grid points are used, it is often desirable to use an individual resolution at each radius which is analyzed. The minimum resolution used in any of the SFINCS runs is $N_\theta = 43$, $N_\phi = 59$ grid points in the poloidal and toroidal direction (per identical segment of the stellarator), $N_\xi = 96$ Legendre polynomials to represent the distribution function and $N_x = 10$ grid points in

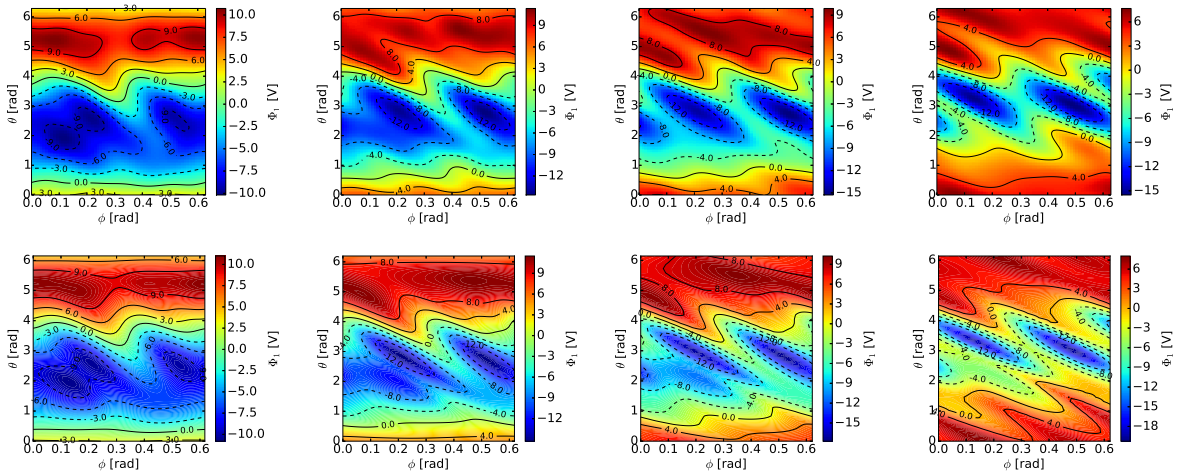

Figure 18: For the LHD A.III profile set, comparison between the potential variation Φ_1 obtained with EUTERPE (top row) and SFINCS (bottom row). The radial positions considered are, from left to right, $r/a = \{0.2, 0.4, 0.6, 0.8\}$.

energy.

The comparison between the calculation by SFINCS and EUTERPE of the electrostatic potential Φ_1 is presented in figure 18. The case considered in this benchmark is the one labelled as A.III in section 3.1 for LHD, and taking the radial positions $r/a = \{0.2, 0.4, 0.6, 0.8\}$ (displayed from left to right). Slight differences are observed between the contour plots, which which can be attributed to the differences noted above. On the other hand the absolute value of the potential is in good agreement. In any case the disagreement is not such that the values of the radial particle flux of carbon C^{6+} obtained by both codes deviate from each other. This is what figure 19 shows, where the circles with error bars show the calculation with EUTERPE and the stars show the results with SFINCS. As in previous figures filled points and solid lines refer to the case including Φ_1 while open points and dashed lines indicate the standard calculation without it.

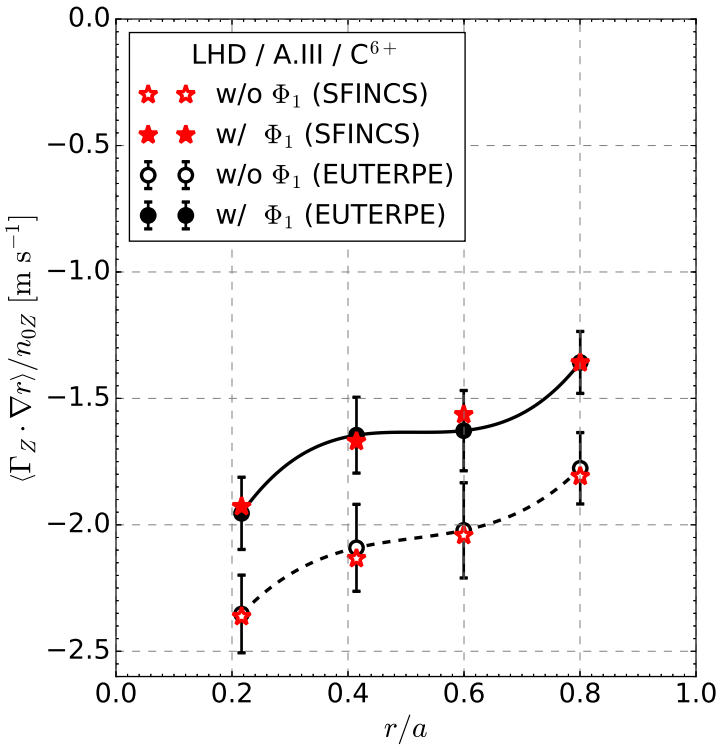

Figure 19: Comparison between EUTERPE (circles) and SFINCS (stars) of the normalized radial particle fluxes of carbon for the case A.III, with (filled points) and without (open points) Φ_1.

References

[1] K Ida *et al.* 2009 Observation of an impurity hole in a plasma with an ion internal transport barrier in the large helical device *Phys. Plasmas* **16** 056111.

[2] M. Yoshinuma *et al.* 2009 Observation of an impurity hole in the large helical device *Nucl. Fusion* **49** 062002.

[3] P. Helander and D. J. Sigmar 2001 *Collisional transport in magnetized plasmas* Cambridge University Press.

[4] P Helander 2014 Theory of plasma confinement in non-axisymmetric magnetic fields. *Rep. Prog. Phys.* **77** 087001.

[5] H Sugama, M. Okamoto, W Horton, and M Wakatani 1996 Transport processes and entropy production in toroidal plasmas with gyrokinetic electromagnetic turbulence. *Phys. Plasmas* **3** 2379.

[6] P Helander and A N Simakov 2008 Intrinsic ambipolarity and rotation in stellarators. *Phys. Rev. Lett.* **101** 145003.

[7] F I Parra, M Barnes, and P J Catto 2011 Sources of intrinsic rotation in the low-flow ordering. *Nucl. Fusion* **51** 113001.

[8] I Calvo and F I Parra Long-wavelength limit of gyrokinetics in a turbulent tokamak and its intrinsic ambipolarity 2012 *Plasma Phys. Contr. Fusion* **56** 099503.

[9] C D Beidler *et al.* 2011 Benchmarking of the mono-energetic transport coefficients–results from the international collaboration on neoclassical transport in stellarators (ICNTS) *Nucl. Fusion* **51** 076001.

[10] F L Hinton and S K Wong 1985 Neoclassical ion transport in rotating axisymmetric plasmas *Phys. Fluids* **28** 3082.

[11] J A Wesson 1997 Poloidal distribution of impurities in a rotating tokamak plasma *Nucl. Fusion* **37** 577.

[12] L C Ingesson, H Chen, P Helander and M J Mantsinen 2000 Comparison of basis functions in soft x-ray tomography and observation of poloidal asymmetries in impurity density *Plasma Phys. and Contr. Fusion* **42** 161.

[13] F L Hinton and M N Rosenbluth 1973 Transport properties of a toroidal plasma at low-to-intermediate collision frequencies *Phys. Fluids* **16** 836.

[14] H E Mynick 1984 Calculation of the poloidal ambipolar field in a stellarator and its effect on transport *Phys. Fluids* **27**(8) 2086.

[15] D D.-M Ho and R M Kulsrud 1987 Neoclassical transport in stellarators *Phys. Fluids* **30**(2) 442.

[16] P Helander 1998 Bifurcated neoclassical particle transport *Phys. Fluids* **5** 3999.

[17] M Romanelli and M Ottaviani 1998 Effects of density asymmetries on heavy impurity transport in a rotating tokamak plasma *Plasma Phys. Contr. Fusion* **40**(10) 1767.

[18] T Fülöp and P Helander 1999 Nonlinear neoclassical transport in a rotating impure plasma with large gradients *Phys. Plasmas* **6** 3066.

[19] C D Beidler and H Maßberg 2005 Implications of the quasi–neutrality condition for neoclassical transport in stellarators In *15th International Stellarator Workshop, Madrid*.

[20] J M García-Regaña *et al.* 2013 On neoclassical impurity transport in stellarator geometry. *Plasma Phys. and Contr. Fusion* **55** 074008.

[21] C Angioni and P Helander 2014 Neoclassical transport of heavy impurities with poloidally asymmetric density distribution in tokamaks *Plasma Phys. and Contr. Fusion* **56**(12) 124001.

[22] M Landreman, H M Smith, A Mollén, and P Helander 2014 Comparison of particle trajectories and collision operators for collisional transport in nonaxisymmetric plasmas *Phys. Plasmas* **21** 042503.

[23] I Calvo, F I Parra, J L Velasco and A Alonso 2016 The effect of tangential drifts on neoclassical transport in stellarators close to omnigeneity *Plasma Phys. Contr. Fusion* submitted.

[24] V Kornilov, R Kleiber, and R Hatzky 2005 Gyrokinetic global electrostatic ion-temperature-

gradient modes in finite β equilibria of Wendelstein 7-x. *Nucl. Fusion* **45**(4) 238.
[25] R Kleiber *et al.* 2011 An improved control-variate scheme for particle-in-cell simulations with collisions *J. Comp. Phys.* **182** 1005.
[26] S Brunner, E Valeo, and J A Krommes 1999 Linear delta-f simulations of nonlocal electron heat transport. *Phys. Plasmas* **6** 4504.
[27] W X Wang, N Nakajima, M Okamoto, and S Murakami 1999 Global δf particle simulation of neoclassical transport and ambipolar electric field in general geometry *Plasma Phys. Contr. Fusion* **41** 1091.
[28] T Takizuka 1977 A binary collision model for plasma simulation with a particle code *J. Comp. Phys.* **25**(3) 205.
[29] K Kauffmann, R Kleiber, R Hatzky, and M Borchardt 2010 Global linear gyrokinetic simulations for lhd including collisions *J. Phys.: Conf. Ser.* **260**(1) 012014.
[30] Y. Turkin *et al.* 2011 Neoclassical transport simulations for stellarators *Phys. Plasmas* **18** 022505.
[31] J Geiger *et al.* 2014 Physics in the magnetic configuration space of W7-X *Plasma Phys. Contr. Fusion* **57** 014004.
[32] S P Hirshman *et al.* 1986 Plasma transport coefficients for nonsymmetric toroidal confinement systems *Phys. Fluids*, **29** 2951.
[33] W. I. van Rij and S. P. Hirshman 1989 Variational bounds for transport coefficients in three-dimensional toroidal plasmas *Phys. Fluids B* **1** 563.
[34] R C Grimm, R L Dewar, and J Manickam 1983 Ideal mhd stability calculations in axisymmetric toroidal coordinate systems *Journal of Computational Physics* **49** 94.
[35] J L Velasco *et al* 2016 Moderation of neoclassical impurity accumulation in high temperature plasmas of helical devices *Nucl. Fusion* (accepted).
[36] C D Beidler and W D D'haeseleer 1995 A general solution of the ripple-averaged kinetic equation (GSRAKE). *Plasma Phys. and Contr. Fusion* **37** 463.
[37] J R Cary and S G Shasharina 1997 Omnigenous stellarators *Plasma Phys. Rep* **23** 509.
[38] J Arévalo, J A Alonso, K J McCarthy, and J L Velasco 2013 Incompressibility of impurity flows in low density tj-ii plasmas and comparison with neoclassical theory *Nucl. Fusion* **53** 023003.
[39] J Arévalo *et al.* 2014 Compressible impurity flow in the tj-ii stellarator *Nucl. Fusion* **54** 013008.
[40] M A Pedrosa *et al.* 2015 Electrostatic potential variations along flux surfaces in stellarators *Nucl. Fusion* **55** 052001.
[41] `https://github.com/landreman/sfincs`
[42] A Mollén, M Landreman, and H M Smith 2014 On collisional impurity transport in nonaxisymmetric plasmas *J. Phys.: Conf. Ser.* **561** 012012.
[43] A Mollén *et al.* 2015 Impurities in a non-axisymmetric plasma: Transport and effect on bootstrap current *Phys. Plasmas* **22** 112508.
[44] M Landreman, H M Smith, A Mollén, and P Helander 2015 20th international stellarator and heliotron workshop.